

1 Why did deep convection persist over four consecutive winters
2 (2015-2018) Southeast of Cape Farewell?

3
4 Patricia ZUNINO¹, Herlé MERCIER² and Virginie THIERRY³.

5 1 Altran Technologies, Technopôle Brest Iroise, Site du Vernis , 300 rue Pierre Rivoalon, 29200 Brest,

6 France

7 2 CNRS, University of Brest, IRD, Ifremer, Laboratoire d'Océanographie Physique et Spatiale (LOPS),

8 IUEM, ZI de la pointe du diable, CS 10070 - 29280 Plouzané, France

9 3 Ifremer, University of Brest, CNRS, IRD, Laboratoire d'Océanographie Physique et Spatiale (LOPS),

10 IUEM, ZI de la pointe du diable, CS 10070 - 29280 Plouzané, France

11
12 Corresponding author: patricia.zuninorodriguez@altran.com

42 **ABSTRACT**

43 After more than a decade of shallow convection, deep convection returned to the Irminger Sea in
44 2008 and occurred several times since then to reach exceptional convection depths (>1,500 m) in
45 2015 and 2016. Additionally, deep mixed layers larger than 1600 m were also reported Southeast of
46 Cape Farewell in 2015. In this context, we used Argo data to show that deep convection occurred
47 Southeast of Cape Farewell (SECF) in 2016 and persisted during two additional years in 2017 and
48 2018 with maximum convection depth larger than 1,300 m. In this article, we investigate the
49 respective roles of air-sea buoyancy flux and preconditioning of the water column (ocean interior
50 buoyancy content) to explain this 4-year persistence of deep convection SECF. We analyzed the
51 respective contributions of the heat and freshwater components. Contrary to the very negative air-
52 sea buoyancy flux that was observed during winter 2015, the buoyancy fluxes over the SECF region
53 during winters 2016, 2017 and 2018 were close to the climatological average. We estimated the
54 preconditioning of the water column as the buoyancy that needs to be removed (B) from the end of
55 summer water column to homogenize it down to a given depth. B was lower for winters 2016 – 2018
56 than for the 2008 – 2015 winter mean, due especially to a vanishing stratification from 600 m down
57 to ~1,300 m. It means that less air-sea buoyancy loss was necessary to reach a given convection
58 depth than in the mean and once convection reached 600 m little additional buoyancy loss was
59 needed to homogenize the water column down to 1,300 m. We showed that the decrease in B was
60 due to the combined effects of the local cooling of the intermediate water (200 – 800 m) and the
61 advection of a negative S anomaly in the 1,200 – 1,400 m layer. This favorable preconditioning
62 permitted the very deep convection observed in 2016 – 2018 despite the atmospheric forcing was
63 close to the climatological average.

64

65

66

67

68

69

70

71 **1. INTRODUCTION**

72 Deep convection is the result of a process by which surface waters lose buoyancy due to
73 atmospheric forcing and sink into the interior of the ocean. It occurs only where specific conditions
74 are met including large air-sea buoyancy loss and favorable preconditioning (i.e. low stratification of
75 the water column) (Marshall & Schott, 1999). In the Subpolar North Atlantic (SPNA), deep convection
76 takes place in the Labrador Sea, South of Cape Farewell and in the Irminger Sea (Kieke & Yashayaev,
77 2015; Pickart et al. 2003; Piron et al. 2017). Deep convection connects the upper and lower limbs of
78 the Meridional Overturning Circulation (MOC) and transfers climate change signals from the surface
79 to the ocean interior.

80 Observing deep convection is difficult because it happens on short time and small spatial scales and
81 during periods of severe weather conditions (Marshall & Schott, 1999). The onset of the Argo
82 program at the beginning of the 2000s has considerably increased the number of available
83 oceanographic data throughout the year. Although the sampling characteristics of Argo are not
84 adequate to observe the small scales associated with the convection process itself, Argo data allow
85 the description of the overall intensity of the event and the characterization of the properties of the
86 water masses formed in the winter mixed layer as well (e.g., Yashayaev and Loder, 2017).

87 In the Labrador Sea, deep convection occurs every year, yet with different intensity (e.g., Yashayaev
88 and Clarke, 2008; Kieke and Yashayaev, 2015). In the Irminger Sea, Argo and mooring data showed
89 that convection deeper than 700 m happened during winters 2008, 2009, 2012, 2015 and 2016 (Våge
90 et al., 2009; de Jong et al., 2012; Piron et al. 2015; de Jong & de Steur, 2016; Fröb et al., 2016; Piron
91 et al. 2017; de Jong et al., 2018). Moreover, in winter 2015, deep convection was also observed south
92 of Cape Farewell (Piron et al., 2017). Excluding winter 2009 when the deep convection event was
93 made possible thanks to a favorable preconditioning (de Jong et al., 2012), all events coincided with
94 strong atmospheric forcing (air-sea heat loss). Prior to 2008, only few deep convection events were
95 reported because the mechanisms leading to it were not favorable (Centurioni and Gould, 2004) or
96 because the observing system was not adequate (Bacon, 1997; Pickart et al., 2003). Nevertheless, the
97 hydrographic properties from the 1990s suggested that deep convection reached as deep as 1,500 m
98 in the Irminger Sea during winters 1994 and 1995 (Pickart et al., 2003), and as deep as 1,000 m south
99 of Cape Farewell during winter 1997 (Bacon et al., 2003).

100 The convection depths that were reached in the Irminger Sea and south of Cape Farewell at the end
101 of winter 2015 were the deepest observed in these regions since the beginning of the 21st century
102 (de Jong et al., 2016; Piron et al., 2017, Fröb et al., 2016). In this work, we show that deep convection

103 also happened in a region between south of Cape Farewell and the Irminger Sea (the pink box in
104 Figure 1) every winter from 2016 to 2018. Hereinafter, we will refer to this region as Southeast Cape
105 Farewell (SECF). We investigated the respective role of atmospheric forcing (air-sea buoyancy flux)
106 and preconditioning (ocean interior buoyancy content) in setting the convection intensity. We also
107 disentangled the relative contribution of salinity and temperature anomalies to the preconditioning.
108 The paper is organized as follow. The data are described in Sect. 2. The methodology is explained in
109 Sect. 3. We expose our results in Sect. 4 and discuss them in Sect. 5. Conclusions are listed in Sect. 6.

110

111 2. DATA

112 We used temperature (T), salinity (S) and pressure (P) data measured by Argo floats north of 55°N in
113 the Atlantic Ocean. These data were collected by the International Argo program
114 (<http://www.argo.ucsd.edu/>), <http://www.jcommops.org/>) and downloaded from the Coriolis Data
115 Center (<http://www.coriolis.eu.org/>). Only data flagged as good (quality Control < 3, Argo Data
116 Management Team, 2017) were considered in our analysis. Potential temperature (θ), density (ρ)
117 and potential density anomaly referenced to the surface and 1000 dbar (σ_0 and σ_1 , respectively) were
118 estimated from T, S and P data using TEOS-10 (<http://www.teos-10.org/>).

119 We used two different gridded products of ocean T and S: ISAS and EN4. ISAS (Gaillard et al., 2016;
120 Kolodziejczyk et al., 2017) is produced by optimal interpolation of *in situ* data. It provides monthly
121 fields, at 152 depth levels, at 0.5° resolution, from 2002 to 2015. Near real time data are also
122 available for 2016 and 2018. EN4 (Good et al., 2013) is an optimal interpolation of *in situ* data; it
123 provides monthly T and S at 1° spatial resolution and at 42 depth levels, for the period 1900 to
124 present.

125 Net air-sea heat flux (Q, the sum of radiative and turbulent fluxes), evaporation (E), precipitation (P),
126 wind stress (τ_x and τ_y) and sea surface temperature (SST) data were obtained from ERA-Interim
127 reanalysis (Dee et al., 2011). ERA-Interim provides data with a time resolution of 12h and a spatial
128 resolution of 0.75°, respectively. The air-sea freshwater flux (FWF) was estimated as E - P.

129 We used monthly Absolute Dynamic Topographic (ADT), which was computed from the daily 0.25° -
130 resolution ADT data provided by CMEMS (Copernicus Marine and Environment Monitoring Service,
131 <http://www.marine.copernicus.eu>).

132

133 3. METHODS

134 3.1 Quantification of the deep convection

135 We characterized the convection in the SPNA in winters 2015-2018 by estimating the mixed layer
136 depths (MLD) for all Argo profiles collected in the SPNA north of 55°N from 1st January to 30th April of
137 each year (Fig. 1). The MLD was estimated as the shallowest of the three MLD estimates obtained by
138 applying the threshold method (de Boyer Montégut et al., 2004) to θ , S and ρ profiles separately. The
139 threshold method computes the MLD as the depth at which the difference between the surface (30
140 m) and deeper levels in a given property is equal to a given threshold. In case visual inspection of the
141 winter profiles showed a thin stratified layer at the surface, a slightly deeper level (<150 m) was
142 considered as surface reference level. Following Piron et al. (2017), this threshold was taken equal to
143 0.01 kg m^{-3} for ρ . For θ and S , we selected thresholds of 0.1°C and 0.012 respectively because they
144 correspond to the threshold of 0.01 kg m^{-3} in ρ . The latter was previously shown to perform well in
145 the subpolar gyre on density profiles (Piron et al., 2016). The criteria on temperature and salinity
146 were chosen to perform well when temperature and salinity anomalies within the density-defined
147 mixed layer are density compensated. Our MLD estimates are comparable to those obtained using
148 MLD determination based on Pickart et al. (2002)'s methods (see section S1, Fig. S1 and Fig. S2 in
149 supplementary material).

150

151 In this paper, deep convection is characterized by profiles with MLD deeper than 700m (colored
152 points in Fig. 1) because it is the minimum depth that should be reached for renewing Labrador Sea
153 Water (LSW) (Yashayaev et al., 2007; Piron et al. 2016). The winter MLD and the associated θ , S and ρ
154 properties were examined for the Labrador Sea and the SECF region by considering the profiles inside
155 the cyan and pink boxes in Fig. 1, respectively. Those two boxes were defined to include all Argo
156 profiles with MLD deeper than 700 m during 2016 – 2018 and the minimum of the monthly ADT for
157 either the SECF region or the Labrador Sea. No deep MLD was recorded in the northernmost part of
158 the Irminger Sea during this period. We computed the maximum MLD and the MLD third quartile
159 (Q_3) from profiles with MLD greater than 700m in each of the two boxes separately. Q_3 is the MLD
160 value that is exceeded by 25% of the profiles and is equivalent to the aggregate maximum depth of
161 convection defined by Yashayaev and Loder (2016). Hereafter, we refer to Q_3 as the aggregate
162 maximum depth of convection. The properties (ρ , θ and S) of the mixed layers were defined for each
163 winter as the vertical mean from 200 m to the MLD of all profiles with MLD deeper than 700 m. For
164 further use, we define the deep convection period as follows. For a given winter, the deep
165 convection period begins the day when the first profile with a deep (>700m) mixed layer is detected
166 and ends the day of the last detection of a deep mixed layer.

167 3.2. Time series of atmospheric forcing

168 The air-sea buoyancy flux (B_{surf}) was calculated as the sum of the contributions of Q and FWF (Gill,
169 1982; Billheimer & Talley, 2013). It reads:

$$170 \quad B_{surf} = \frac{\alpha g}{\rho_0 c_p} Q - \beta g SSS FWF \quad \text{Eq. (1)}$$

171 Where α and β are the coefficients of thermal and saline expansions, respectively, estimated from
172 surface T and S. The gravitational acceleration g is equal to 9.8 m s^{-2} , the reference density of sea
173 water ρ_0 is equal to 1026 kg m^{-3} and heat capacity of sea water C_p is equal to $3990 \text{ J kg}^{-1} \text{ }^\circ\text{C}^{-1}$. SSS is
174 the sea surface salinity. Q and FWF are in W m^{-2} and m s^{-1} , respectively.

175 For easy comparison with previous results, which only considered the heat component of the
176 buoyancy air-sea flux (e.g. Yashayaev & Loder, 2017; Piron et al. 2017; Rhein et al., 2017), B_{surf} in m^2
177 s^{-3} , was converted to W m^{-2} following Eq. (2) and noted B_{surf}^*

$$178 \quad B_{surf}^* = \frac{\rho_0 c_p}{g \alpha} B_{surf} \quad \text{Eq. (2)}$$

179 The FWF was also converted to W m^{-2} using:

$$180 \quad FWF^* = FWF \beta SSS \frac{\rho_0 c_p}{\alpha} \quad \text{Eq. (3)}$$

181 We also computed the horizontal Ekman buoyancy flux (BF_{ek}), which can be decomposed into the
182 horizontal Ekman heat flux (HF_{ek}) and salt flux (SF_{ek}). Noting :

$$183 \quad BF_{ek} = -g (U_e \partial_x SSD + V_e \partial_y SSD) \frac{C_p}{\alpha g} \quad \text{Eq. (4)}$$

$$184 \quad HF_{ek} = -(U_e \partial_x SST + V_e \partial_y SST) \rho_0 C_p \quad \text{Eq. (5)}$$

$$185 \quad SF_{ek} = -(U_e \partial_x SSS + V_e \partial_y SSS) \frac{\beta \rho_0 C_p}{\alpha} \quad \text{Eq. (6)}$$

186 $BF_{ek} = SF_{ek} - HF_{ek}$. U_e and V_e are the eastward and northward components of the Ekman horizontal
187 transport estimated from the wind stress meridional and zonal components. SSD, SST and SSS are ρ ,
188 T and S at the surface of the ocean. BF_{ek} , HF_{ek} and SF_{ek} are in $\text{J s}^{-1} \text{ m}^{-2}$. Because ERA-Interim does not
189 supply SSD or SSS, they were estimated from EN4 as follows. The monthly T and S data at 5 m depth
190 from EN4 were interpolated on the same time and space grid as the air-sea fluxes from ERA-Interim
191 (12h and 0.75° , respectively). SSD was estimated from those interpolated EN4 data (SST and SSS).
192 Properties at 5 m depth were considered to be representative of the Ekman layer. Data at locations

193 where ocean bottom was shallower than 1000 m were excluded from the analysis to avoid regions
194 covered by sea-ice.

195 Following Piron et al. (2016), the time series of atmospheric forcing were estimated for the SECF
196 region and the Labrador Sea as follows. First, the gridded air-sea flux data and the horizontal Ekman
197 fluxes were averaged over the pink (SECF region) and cyan (Labrador Sea) boxes (Fig. 1). Second, we
198 estimated the accumulated fluxes from 1 September to 31 August the year after. Finally, we
199 computed the time series of the anomalies of the accumulated fluxes from 1 September to 31 August
200 with respect to the 1993 – 2016 mean.

201 Finally, in order to quantify the net intensity of the atmospheric forcing over the winter, we
202 computed estimates of $B_{\text{surf}}^* + BF_{\text{ek}}$ fluxes accumulated from 1 September to 31 March the year after.
203 Following Piron et al. (2017), the associated errors were calculated by a Monte Carlo simulation using
204 50 random perturbations of Q, FWF and B_{surf} . The error amounted to 0.05, 0.04 and 0.03 J m⁻² for
205 B_{surf}^* , Q and FWF*, respectively. The error of the horizontal Ekman buoyancy transport was also
206 estimated by a Monte Carlo simulation and amounted to 0.04 J m⁻².

207 3.3. Preconditioning of the water column

208 The preconditioning of the water column was evaluated as the buoyancy that has to be removed
209 ($B(z_i)$) from the late summer density profile to homogenize it down to a depth z_i . It reads:

$$210 \quad B(z_i) = \frac{g}{\rho_0} \sigma_0(z_i) z_i - \frac{g}{\rho_0} \int_{z_i}^0 \sigma_0(z) dz \quad \text{Eq. (7)}$$

211 $\sigma_0(z)$ is the vertical profile of potential density anomaly estimated from the profiles of T and S
212 measured by Argo floats in September in the given region (pink or cyan box in Fig. 1).

213 Following Schmidt and Send (2007), we split B into a temperature (B_θ) and salinity (B_S) term:

$$214 \quad B_\theta(z_i) = - (g \alpha \theta(z_i) z_i - g \alpha \int_{z_i}^0 \theta(z) dz) \quad \text{Eq. (8)}$$

$$215 \quad B_S(z_i) = g \beta S(z_i) z_i - g \beta \int_{z_i}^0 S(z) dz \quad \text{Eq. (9)}$$

216 In order to compare the preconditioning with the heat to be removed and/or air-sea heat fluxes, B ,
217 B_θ and B_S are reported in J m⁻². B , B_θ and B_S were estimated for a given year from the mean of all
218 September profiles of B , B_θ and B_S . The associated errors were estimated as $\text{std}(B)/\sqrt{n}$, where n is
219 the number of profiles used to compute the September mean values.

220

221 4. RESULTS

222 4.1. Intensity of deep convection and properties of newly formed LSW

223 We examine the time-evolution of the winter mixed layer SECF since the exceptional convection
224 event of winter 2015 (W2015 hereinafter) (Table 1 and Figs. 1 - 3). In W2015, we recorded a
225 maximum MLD of 1,710 m south of Cape Farewell (Fig. 1a), in line with Piron et al. (2017). The
226 maximum MLD of 1,575 m observed for W2016 (Fig. 1b) is compatible with the active mixed layer >
227 1,500 m observed in a mooring array in the central Irminger Sea by de Jong et al. (2018). For W2015
228 and W2016, the aggregate maximum depth of convection was 1,205 m and 1,471 m, respectively
229 (Table 1). In W2017, deep convection was observed from three Argo profiles (Fig. 1c and Fig. 2a-c).
230 The maximum MLD of 1,400 m was observed on 16th March 2017 at 56.65°N – 42.30°W. In W2018,
231 the maximum MLD of 1,300 m was observed on 24 February at 58.12°N, 41.84°W (Fig. 1d, 2d-f). Float
232 5903102 measured MLD of 1,100 m South of Cape Farewell (Fig. 1d), but the estimated MLDs
233 coincided with the deepest levels of measurement of the float so that these estimates, possibly
234 biased low (see Fig. 2d-f), were discarded from our analysis. These results show that convection
235 deeper than 1,300 m occurred during four consecutive winters SECF.

236 Although the number of floats showing deep convection in W2017 and W2018 was small (3 and 2
237 floats), it represented a significant percentage of the floats operating in the SECF box at that time.
238 The percentage of floats showing deep convection in the SECF region was computed for the deep
239 convection periods defined from 15 January 2015 to 21 April 2015, 22 February 2016 to 21 March
240 2016, 16 March 2017 to 4 April 2017 and 24 February 2018 to 26 March 2018. The longest period of
241 deep convection occurred in W2015, the shortest in 2017. The percentage of floats showing deep
242 convection during the deep convection period are 73%, 50%, 33 % and 50%, for winters 2015, 2016,
243 2017 and 2018, respectively. The lowest % is found for W2017, but it is still substantial. It might
244 reflect that for this specific year floats showing deep MLD were found in the southwestern corner of
245 the SECF box only, suggesting that convection did not occur over the full box.

246 The properties (σ_0 , S and θ) of the end of winter mixed layer were estimated for the four winters
247 (Table 1 and Fig. 3). We observed that, between W2015 and W2018, the water mass formed by deep
248 convection significantly densified and cooled by 0.019 kg m^{-3} and 0.215°C , respectively (see Table 1
249 and Fig. 3).

250 In the Labrador Sea, the aggregate maximum depth of convection increased from 2015 to 2018 (see
251 Table 1). Deep convection observed in the Labrador Sea in W2018 was the most intense since the
252 beginning of the Argo era (see Fig. 2c in Yashayaev & Loder, 2016). From W2015 to W2018, newly

253 formed LSW cooled, became saltier and densified by 0.134°C, 0.013 and 0.023 kg m⁻³, respectively
254 (Table 1).

255 The water mass formed SECF is warmer and saltier than that formed in the Labrador Sea (Fig. 3). The
256 deep convection SECF is always shallower than in the Labrador Sea. This result is discussed later in
257 Sect. 5.

258 4.2. Analysis of the atmospheric forcing Southeast of Cape Farewell

259 The seasonal cycles of B_{surf}^* and Q are in phase and of the same order of magnitude, while FWF^* ,
260 which is positive and one order of magnitude lower than Q , does not present a seasonal cycle (Fig.
261 S3). The means (1993 – 2018) of the cumulative sums from 1 September to 31 March of Q , FWF^* and
262 B_{surf}^* estimated over the SECF box (Fig. 1) are $-2.46 \pm 0.43 \times 10^9 \text{ J m}^{-2}$, $0.28 \pm 0.10 \times 10^9 \text{ J m}^{-2}$ and
263 $-2.22 \pm 0.49 \times 10^9 \text{ J m}^{-2}$, respectively. B_{surf}^* is 10 % lower on average than Q because of the buoyancy
264 addition by FWF^* . Considering the Ekman transports, the 1993 – 2018 means of the accumulated
265 BF_{ek} , HF_{ek} and SF_{ek} from 1 September to 31 March amount to $0.37 \pm 1.15 \times 10^8 \text{ J m}^{-2}$, $-0.35 \pm 1.36 \times$
266 10^8 J m^{-2} , and $0.02 \pm 2.04 \times 10^8 \times 10^9 \text{ J m}^{-2}$, respectively. The horizontal Ekman heat flux is negative,
267 while the Ekman buoyancy flux is positive. This buoyancy gain indicates a southeastward transport of
268 surface freshwater caused by dominant winds from the southwest. Noteworthy, BF_{ek} is one order of
269 magnitude smaller than the B_{surf}^* .

270 The total atmospheric forcing SECF was quantified as the sum of B_{surf}^* and BF_{ek} . The anomalies of
271 accumulated fluxes from 1 September to 31 August the year after, with respect to the mean 1993 –
272 2016, are displayed in Fig. 4 for the SECF box. The grey line in Fig. 4a is the total atmospheric forcing
273 anomaly (B_{surf}^* plus BF_{ek}). We identify years with very negative buoyancy loss in the SECF region, e.g.
274 1994, 1999, 2008, 2012 and 2015. The very negative anomalies of atmospheric forcing in 1999 and
275 2015 were caused by the very negative anomalies in both B_{surf}^* (Fig. 4a) and BF_{ek} (Fig.4d). This
276 correlation was not observed for all the years presenting a negative anomaly of atmospheric forcing.
277 Noteworthy, during W2016, W2017 and W2018, the anomaly of atmospheric forcing was close to
278 zero.

279 Contrary to the very negative anomaly in atmospheric fluxes over the SECF region observed for
280 W2015, the atmospheric fluxes were close to the mean during W2016, W2017 and W2018.

281 4.3. Analysis of the preconditioning of the water column Southeast of Cape 282 Farewell

283 Our hypothesis is that the exceptional deep convection that happened in W2015 in the SECF region
284 favorably preconditioned the water column for deep convection the following winters. The time-
285 evolutions of θ , S , σ_1 and of $\Delta\sigma_1=0.01 \text{ kg m}^{-3}$ layer thicknesses (Fig. 5) show a marked change in the
286 hydrographic properties of the SECF region at the beginning of 2015 caused by the exceptional deep
287 convection that occurred during W2015 (see Piron et al., 2017). The intermediate waters (500 –
288 1,000 m) became colder than the years before and, despite a slight decrease in salinity, the cooling
289 caused the density to increase (Fig. 5c). Fig. 5d shows $\Delta\sigma_1=0.01 \text{ kg m}^{-3}$ layer thicknesses larger than
290 600 m appearing at the end of W2015 for the first time since 2002. In the density range 32.36 – 32.39
291 kg m^{-3} , these layers remained thicker than ~450 m during W2016 to W2018. This indicates low
292 stratification at intermediate depths and a favorable preconditioning of intermediate waters for deep
293 convection initiated by W2015 deep convection. The denser density of the core of the thick layers in
294 2017 -2018 compared with 2015 - 2016 agrees with the densification of the mixed layer SECF shown
295 in Table 1 and Fig. 3.

296 $B(z_i)$ is our estimate of the preconditioning of the water column before winter (see Method). Fig. 6a
297 shows that, deeper than 100 m, B for W2016, W2017 and W2018 was smaller than B for W2015 or B
298 for the mean W2008 – W2014. Furthermore, for W2016, W2017 and 2018, B remained nearly
299 constant with depth between 600 and 1,300 m, which means that once the water column has been
300 homogenized down to 600 m, little additional buoyancy loss results in the homogenization of the
301 water column down to 1,300 m. Both conditions (i) less buoyancy to be removed and (ii) absence of
302 gradient in the B profile down to 1,300 m indicate a more favorable preconditioning of the water
303 column for W2016, W2017 and W2018 than during W2008 – W2015.

304 To understand the relative contributions of θ and S to the preconditioning, we computed the thermal
305 (B_θ) and haline (B_s) components of B ($B = B_\theta + B_s$). In general, B_θ (B_s) increases with depth when θ
306 decreases (S increases) with depth. On the contrary, a negative slope in a B_θ (B_s) profile corresponds
307 to θ increasing (S decreasing) with depth and is indicative of a destabilizing effect. The negative
308 slopes in B_θ and B_s profiles are not observed simultaneously because density profiles are stable.

309 We describe the relative contributions of B_θ and B_s to B by looking first at the mean 2008 – 2014
310 profiles (discontinuous blue lines in Fig. 6). B_θ accounts for most of the increase in B from the surface
311 to 800 m and below 1,400 m (see Fig. 6a and Fig. 6b). The negative slope in the B_s profile between
312 800 – 1,000 m (Fig. 6c) slightly reduces B (Fig. 6a) and is due to the decrease in S associated with the
313 core of LSW (see Fig. 3 in Piron et al. 2016). In the layer 1,000 – 1,400 m, the increase in B (Fig. 6a) is
314 mainly explained by the increase in B_s (Fig. 6c), which follows the increase in S in the transition from
315 LSW to Iceland Scotland Overflow Water (ISOW). This transition layer will be referred to hereinafter

316 as the deep halocline. The evaluation of the preconditioning of the water column was usually
317 analyzed in terms of heat (e.g., Piron et al. 2015; 2017). The decomposition of B in B_θ and B_S reveals
318 that θ governs B in the layer 0 – 800 m. S tends to reduce the stabilizing effect of θ in the layer 800 –
319 1,000 m, and reinforces it in the layer 1,000 – 1,400 m by adding up to $1 \times 10^9 \text{ J m}^2$ to B .

320 In order to further understand why the SEFC region was favorably preconditioned during winters
321 2016 – 2018, we compare the B_θ and B_S of W2017, which was the most favorably preconditioned
322 winter, with the mean 2008 – 2014 (Fig. 7a). From the surface to 1,600 m, B_θ and B_S were smaller for
323 W2017 than for the mean 2008 – 2014. There are two additional remarkable features. First, in the
324 layer 500 – 1000 m, the large reduction of B_θ compared to the 2008 – 2014 mean, mostly explains
325 the decrease in B in this layer. Second, the more negative value of B_S in the layer 1,100 – 1,300 m,
326 compared to the 2008 – 2014 mean, eroded the B_θ slope, making the B profile more vertical for
327 W2017 than for the mean. The more negative contribution of B_S in the layer 1,100 – 1,300 m comes
328 from the fact that the deep halocline was deeper for W2017 (1,300 m, see orange dashed line in Fig.
329 7a) than for the mean 2008 – 2014 (1,000 m, see blue dashed line in Fig. 7a). Finally, we note that the
330 profiles of $B(z_i)$, $B_\theta(z_i)$ and $B_S(z_i)$ for W2016 and W2018 are more similar to the profiles of W2017 than
331 to those of W2015 or to the mean 2008 – 2014 (see Fig. 6), which indicates that the water column
332 was also favorably preconditioned for deep convection in W2016 and W2018 for the same reasons as
333 in W2017.

334 The origin of the changes in B is now discussed from the time evolutions of the monthly anomalies of
335 θ , S and σ_0 at $58^\circ\text{N} - 40^\circ\text{W}$ that is at the center of the SECF box (Fig. 8). The time evolutions there are
336 similar to those at any other location inside the SECF box. These anomalies were computed using
337 ISAS (Gaillard et al., 2016) and were referenced to the monthly mean of 2002 – 2016. A positive
338 anomaly of σ_0 appeared in 2014 between the surface and 600 m (Fig. 8a) and reached 1,200m in
339 2015 and beyond. This positive anomaly of σ_0 correlates with a negative anomaly of θ . The latter,
340 however, reached $\sim 1,400$ m depth in 2016 that is deeper than the positive anomaly of σ_0 . The
341 negative anomaly of S between 1,000 - 1,500 m that appeared in 2015 and strongly reinforced in
342 2016 caused the negative anomaly in σ_0 between 1,200 – 1,500 m (the density anomaly caused by
343 the negative anomaly in θ between 1,200 – 1,400 m does not balance the density anomaly caused by
344 the negative anomaly of S).

345 The θ and S anomalies in the water column during 2016 – 2018 explain the anomalies of B , B_θ and B_S
346 and can be summarized as follows. On the one hand, the properties of the surface waters (down to
347 500 m) were colder than previous years and, despite they were also fresher, they were denser. The
348 density increase in the surface water reduced the density difference with the deeper-lying waters.

349 The intermediate layer (500 – 1000 m) was also favorably preconditioned due to the observed
350 cooling. Additionally, in the layer 1,100 – 1,300 m, the large negative anomaly of B_s with respect to its
351 mean is explained by the decrease in S in this layer, which caused a decrease in σ_θ and, consequently,
352 reduced the σ_θ difference with the shallower-lying water. The decrease in S also resulted in a
353 deepening of the deep halocline.

354 4.4. Atmospheric forcing versus preconditioning of the water column

355 We now use the estimates of the accumulated atmospheric forcing ($B_{\text{surf}}^* + BF_{\text{ek}}$) from 1 September
356 to 31 March the year after (see Fig. S4) to predict the maximum convection depth for a given winter
357 based on September profiles of B . The predicted convection depth is determined as the depth at
358 which $B(z_i)$ (Fig. 6a) equals the accumulated atmospheric forcing. The associated error was estimated
359 by propagating the error in the atmospheric forcing ($0.05 \times 10^9 \text{ J m}^{-2}$). The accumulated atmospheric
360 forcing amounted to $-3.21 \times 10^9 \pm 0.05 \text{ J m}^{-2}$, $-2.21 \pm 0.04 \times 10^9 \text{ J m}^{-2}$, $-2.01 \pm 0.05 \times 10^9 \text{ J m}^{-2}$ and -2.47
361 $\pm 0.05 \times 10^9 \text{ J m}^{-2}$ for W2015, W2016, W2017 and W2018, respectively. We found predicted
362 convection depths of $1,085 \pm 20 \text{ m}$, $1,285 \pm 20 \text{ m}$, $1,415 \pm 20 \text{ m}$ and $1,345 \pm 20 \text{ m}$ for W2015, W2016,
363 W2017 and W2018, respectively. We consider the aggregate maximum depth of convection as the
364 observed estimate of the MLD (Table 1). The predicted MLD agrees with the observed MLD within \pm
365 200 m. The differences could be due to errors in the atmospheric forcing (Josey et al., 2018), lateral
366 advection and/or spatial variation in the convection intensity within the box not captured by the
367 Argo sampling.

368 The satisfactory predictability of the convection depth with our 1-D model indicates that deep
369 convection occurred locally. In spite the atmospheric forcing was close to mean (1993 – 2016)
370 conditions during W2016, W2017 and W2018, convection depths $> 1300 \text{ m}$ were reached in the SECF
371 region. This was only possible thanks to the favorable preconditioning.

372

373 5. DISCUSSION

374 Deep convection happens in the Irminger Sea and South of Cape Farewell during specific winters
375 characterized by a strong atmospheric forcing (high buoyancy loss), a favorable preconditioning (low
376 stratification) or both at the same time (Bacon et al., 2003; Pickart et al., 2003). In the Irminger Sea,
377 strong atmospheric forcing explained for instance the very deep convection (reaching depth greater
378 than 1,500 m) observed in the early 90s (Pickart, et al., 2003) and in W2015 (de Jong et al. 2016; Fröb
379 et al., 2016; Piron et al. 2017). It explained as well the return of deep convection in W2008 (Väge et
380 al., 2009) and in W2012 (Piron et al., 2016). The favorable preconditioning caused by the
381 densification of the mixed layer during W2008 favored a new deep convection event in W2009

382 despite neutral atmospheric forcing (de Jong et al. 2012). Similarly, the preconditioning observed
383 after W2015 in the SECF region favored deep convection in W2016 (this work). The favorable
384 preconditioning persisted three consecutive winters (2016 – 2018) in the SECF region, which allowed
385 deep convection although atmospheric forcing was close to the climatological values. Why did this
386 favorable preconditioning persist in time?

387 We previously showed that during 2016 – 2018 two hydrographic anomalies affected different
388 ranges of the water column in SECF box: a cooling intensified in the layer 200 – 800 m and a
389 freshening intensified in 1,000 – 1,500 m layer. Those resulted in a decrease in the vertical density
390 gradient between the intermediate and the deeper layers creating a favorable preconditioning of the
391 water column. Note that the cooling affected the layer from surface to 1,400 m and the freshening
392 affected the layer from near surface to 1,600 m, but the cooling and the freshening were intensified
393 at different depth ranges (Fig. 8).

394 We see in Fig. 5a a sudden decrease in θ in the intermediate layers in 2015 compared to the previous
395 years. It indicates that the decrease in θ of the intermediate layer likely originated locally during
396 W2015 when extraordinary deep convection happened. A slight freshening of the water column
397 (400- 1,500 m) appeared in 2015, likely caused by the W2015 convection event, then it decreased
398 before a second S anomaly intensified in 2016 between 1,100 and 1,400 m (Fig. 8c). It is unlikely that
399 this second anomaly was exclusively locally formed by deep convection because it intensified during
400 summer 2016. Our hypothesis is that this second S anomaly originated in the Labrador Sea and was
401 further transferred to the SECF region by the cyclonic circulation encompassing the Labrador Sea and
402 Irminger Sea at these depths (Daniault et al., 2016; Ollitrault & Colin de Verdière, 2014; Lavander et
403 al., 2000 ; Straneo et al., 2003). It is corroborated by the 2D evolution of the anomalies in S in the
404 layer 1,200 – 1,400 m (Fig. 9): a negative anomaly in S appeared in the Labrador Sea in February
405 2015, which was transferred southward and northeastward in February 2016 and intensified over the
406 whole SPNA in February 2017. By this mechanism, the advection from the Labrador Sea contributed
407 to create property anomalies in the water column. However, the buoyancy budget showed that this
408 was a minor contribution compared to the buoyancy loss due to the local air-sea flux, even if it was
409 essential to preconditioning the water column for deep convection.

410 We now compare the atmospheric forcing and the preconditioning of the water column in the SECF
411 region with those of the nearby Labrador Sea where deep convection happens almost every year.
412 The atmospheric forcing over the Labrador Sea is $\sim 15\%$ larger than that over the SECF region: the
413 means (1993 - 2018) of the atmospheric forcing, defined as the time accumulated $B_{\text{surf}}^* + BF_{\text{ek}}$ from 1
414 September to 31 March the year after, are $-2.61 \pm 0.55 \times 10^9 \text{ J m}^{-2}$ in the Labrador Sea and $-2.18 \pm$

415 $0.54 \times 10^9 \text{ J m}^{-2}$ in the SECF region. The difference was larger during the period 2016 – 2018 when the
416 atmospheric forcing equaled $-3.10 \pm 0.19 \times 10^9 \text{ J m}^{-2}$ in the Labrador Sea and $-2.23 \pm 0.23 \times 10^9 \text{ J m}^{-2}$ in
417 the SECF region. In terms of preconditioning, the 2008 – 2014 mean B profile (blue continuous lines
418 in Fig. 7) was lower by $\sim 0.5 \times 10^9 \text{ J m}^{-2}$ in the Labrador Sea than SECF for the surface to 1,000 m layer
419 and by more than $1 \times 10^9 \text{ J m}^{-2}$ below 1,200 m. It indicates that the water column was more favorably
420 preconditioned in the Labrador Sea than in the SECF region during 2008 – 2014. Differently, B for
421 W2017 shows slightly lower values from the surface to 1,300 m in the SECF region than in the
422 Labrador Sea (see orange lines in Fig. 7). However, B in the Labrador Sea remains constant down to
423 the depth of the deep halocline between LSW and North Atlantic Deep Water (NADW) at 1,700 m. In
424 the SECF region, the deep halocline remained at $\sim 1,300$ m between 2016 and 2018 (see B_s lines in
425 Fig. 7a). Differently, in the Labrador Sea, the deep halocline deepened from 1,200 m for the mean to
426 1,735 m, 1,775 m and 1905 m in W2016, W2017 and W2018, respectively (see dashed lines in Fig.
427 7b). The deep halocline acts as a physical barrier for deep convection in both the SECF region and the
428 Labrador Sea, but because the deep halocline is deeper in the Labrador Sea than in SECF region, the
429 preconditioning is more favorable to a deeper convection in the Labrador Sea than in the SECF
430 region. Summarizing, in winters 2016 - 2018 in the Labrador Sea, both atmospheric forcing and
431 preconditioning of the water column granted the deepest convection depth in the Labrador Sea since
432 the beginning of the Argo period (comparison of our results with those of Yashayaev and Loader,
433 2017). Contrasting, in SECF region, during the same period, the atmospheric forcing was close to
434 climatological values, and the favorable preconditioning of the water column allowed 1,300 m depth
435 convection, what was exceptional for the SECF region.

436 The Labrador Sea, SECF region and Irminger Sea are three distinct deep convection sites (e.g.
437 Yashayaev et al., 2007; Bacon et al., 2003; Pickart et al., 2003; Piron et al., 2017). In this work, we
438 give new insights on the connections between the different sites, showing how lateral advection of
439 fresh LSW formed in the Labrador Sea favored the preconditioning in the SECF region fostering
440 deeper convection.

441 Climate models forecast increasing input of freshwater in the North Atlantic due to ice-melting under
442 present climate change (Bamber et al., 2018), which could reduce, or even shut-down, the deep
443 convection in the North Atlantic (Yang et al., 2016; Brodeau & Koenigk, 2016). We observed a fresh
444 anomaly in the surface waters in regions close to the eastern coast of Greenland in 2016 that
445 extended to the whole Irminger Sea in 2017 (Fig. S6). However, this surface freshening did not
446 hamper the deep convection in the SECF region possibly because the surface water also cooled.
447 Swingedouw et al., 2013 indicated that the freshwater signal due to Greenland ice sheet melting is
448 mainly accumulating in the Labrador Sea. However, no negative anomaly of S was detected in the

449 surface waters of the Labrador Sea (Fig. S6). It might be explained by the intense deep convection
450 affecting the Labrador Sea since 2014 that could have transferred the surface freshwater anomaly to
451 the ocean interior. This suggests that, in the last years, the interactions between expected climate
452 change anomalies and the natural dynamics of the system combined to favor very deep convection.
453 This however does not foretell the long term response to climate change.

454

455 **6. CONCLUSIONS**

456 During 2015 – 2018 winter deep convection happened in the SECF region reaching deeper than 1,300
457 m. The deep convection of W2015 was observed over a larger region and during a longer period of
458 time than the deep convection events of winters 2016, 2017 and 2018. Despite these differences, it is
459 the first time that deep convection, with maximum convection depth larger than 1,300 m, was
460 observed in this region during four consecutive winters.

461 The atmospheric forcing and preconditioning of the water column was evaluated in terms of
462 buoyancy. We showed that the atmospheric forcing is 10% weaker when evaluated in terms of
463 buoyancy than in terms of heat because of the non-negligible effect of the freshwater flux. The
464 analysis of the preconditioning of the water column in terms of buoyancy to be removed (B) and its
465 thermal and salinity terms (B_θ and B_s) revealed that B_θ dominated the B profile from the surface to
466 800 m and B_s reduced the B in the 800 – 1000 m layer because of low salinity of LSW. Deeper, B_s
467 increased B due to the deep halocline (LSW-ISOW) that acted as a physical barrier limiting the depth
468 of the convection.

469 During 2016 – 2018, the air-sea buoyancy losses were close to the climatological values and the very
470 deep convection was possible thanks to the favorable preconditioning of the water column. It was
471 surprising that these events reached convection depths similar to those observed in W2012 and
472 W2015, when the latter were provoked by high air-sea buoyancy loss intensified by the effect of
473 strong wind stress. It was also surprising that the water column remained favorably preconditioned
474 during three consecutive winters without strong atmospheric forcing. In this paper, we studied the
475 reasons why this happened.

476 The preconditioning for deep convection during 2016 – 2018 was particularly favorable due to the
477 combination of two types of hydrographic anomalies affecting different depth ranges. First, the
478 surface and intermediate waters (down to 800 m) were favorably preconditioned because buoyancy
479 (density) decreased (increased) due to the cooling caused by the atmospheric forcing. Second,

480 buoyancy (density) increased (decreased) in the layer 1,200 – 1,400 m due to the decrease in S
481 caused by the lateral advection of fresher LSW formed in the Labrador Sea. The S anomaly of this
482 layer resulted in a deeper deep halocline. Hence, the cooling of the intermediate water was essential
483 to reach convection depth of 800 – 1,000 m, and the freshening in the layer 1,200 – 1,400 m and the
484 associated deepening of the deep halocline, allowed the very deep convection (> 1,300 m) in W2016
485 – W2018.

486 **Author contribution:** PZ treated and analyzed the data. PZ and HM interpreted the results. PZ, HM
487 and VT discussed the results and wrote the paper.

488 **ACKNOWLEDGEMENT**

489 This paper is a contribution to the EQUIPEX NAOS project funded by the French National Research
490 Agency (ANR) under reference ANR-10-EQPX-40. The Argo data were collected and made freely
491 available by the International Argo Program and the national programs that contribute to
492 it. (<http://www.argo.ucsd.edu>, <http://argo.jcommops.org>). The Argo Program is part of the Global
493 Ocean Observing System. The NAO data were downloaded from the UCAR Climate Data Guide
494 website (Schneider et al., 2013): [https://climatedataguide.ucar.edu/climate-data/hurrell-north-](https://climatedataguide.ucar.edu/climate-data/hurrell-north-atlantic-oscillation-nao-index-pc-based)
495 [atlantic-oscillation-nao-index-pc-based](https://climatedataguide.ucar.edu/climate-data/hurrell-north-atlantic-oscillation-nao-index-pc-based). The Ssalto/Duacs altimeter products were produced and
496 distributed by the Copernicus Marine and Environment Monitoring Service (CMEMS)
497 (<http://www.marine.copernicus.eu>). We thank F. de Jong and two anonymous reviewers, their
498 comments and suggestions have enriched our work.

499

500 **REFERENCES**

- 501 Argo Data Management Team: Argo user's manual V3.2. <https://doi.org/10.13155/29825>, 2017
- 502 Argo group: Argo float data and metadata from Global Data Assembly Centre (Argo GDAC),
503 SEANOE, <https://doi.org/10.17882/42182,2019>
- 504 Bacon, S.: Circulation and Fluxes in the North Atlantic between Greenland and Ireland. *Journal of*
505 *Physical Oceanography*, 27(7), 1420–1435. [https://doi.org/10.1175/1520-](https://doi.org/10.1175/1520-0485(1997)027<1420:CAFITN>2.0.CO;2)
506 [0485\(1997\)027<1420:CAFITN>2.0.CO;2](https://doi.org/10.1175/1520-0485(1997)027<1420:CAFITN>2.0.CO;2), 1997.
- 507 Bacon, S., Gould, W. J. and Jia, Y.: Open-ocean convection in the Irminger Sea, *Geophys. Res. Lett.*,
508 30(5), 1246, doi:10.1029/2002GL016271, 2003.
- 509 Bamber, J. L., Tedstone, A. J., King, M. D., Howat, I. M., Enderlin, E. M., van den Broeke, M. R., & Noel,

510 B.: Land Ice Freshwater Budget of the Arctic and North Atlantic Oceans: 1. Data, Methods, and
511 Results, *Journal of Geophysical Research: Oceans*, 1–11,
512 <https://doi.org/10.1002/2017JC013605>, 2018.

513 Billheimer, S., & Talley, L. D.: Near cessation of Eighteen Degree Water renewal in the western North
514 Atlantic in the warm winter of 2011 – 2012, *118*(November), 6838–6853,
515 <https://doi.org/10.1002/2013JC009024>, 2013.

516 Brodeau, L., & Koenigk, T.: Extinction of the northern oceanic deep convection in an ensemble of
517 climate model simulations of the 20th and 21st centuries, *Climate Dynamics*, *46*(9–10), 2863–
518 2882. <https://doi.org/10.1007/s00382-015-2736-5>, 2016.

519 Centurioni and Gould, W. J.: Winter conditions in the Irminger Sea observed with profiling floats,
520 *Journal of Marine Research*, *62*, 313–336, 2004.

521 Daniault, N., Mercier, H., Lherminier, P., Sarafanov, A., Falina, A., Zunino, P., Gladyshev, S. : The
522 northern North Atlantic Ocean mean circulation in the early 21st century, *Progress in*
523 *Oceanography*, *146*(June), 142–158, <https://doi.org/10.1016/j.pocean.2016.06.007>, 2016.

524 de Boyer Montégut, C., Madec, G., Fischer, A. S., Lazar, A., & Iudicone, D.: Mixed layer depth over the
525 global ocean: An examination of profile data and a profile-based climatology, *Journal of*
526 *Geophysical Research C: Oceans*, *109*(12), 1–20, <https://doi.org/10.1029/2004JC002378>, 2004.

527 de Jong, M.F., Oltmanns, M., Karstensen, J., and de Steur, L.: Deep Convection in the Irminger Sea
528 Observed with a Dense Mooring Array, *31*(February), 50–59,
529 <https://doi.org/10.5670/oceanog.2018.109>, 2018.

530 de Jong, M. F., & de Steur, L.: Strong winter cooling over the Irminger Sea in winter 2014–2015,
531 exceptional deep convection, and the emergence of anomalously low SST, *Geophysical*
532 *Research Letters*, *43*(13), 7106–7113. <https://doi.org/10.1002/2016GL069596>, 2016.

533 de Jong, M. F., Van Aken, H. M., Våge, K., & Pickart, R. S.: Convective mixing in the central Irminger
534 Sea: 2002-2010, *Deep-Sea Research Part I: Oceanographic Research Papers*, *63*, 36–51.
535 <https://doi.org/10.1016/j.dsr.2012.01.003>, 2012.

536 Dee, D. P., Uppala, S. M., Simmons, A. J., Berrisford, P., Poli, P., Kobayashi, S., Vitart, F.: The ERA-
537 Interim reanalysis: Configuration and performance of the data assimilation system, *Quarterly*
538 *Journal of the Royal Meteorological Society*, *137*(656), 553–597. <https://doi.org/10.1002/qj.828>,
539 2011.

540 Fröb, F., Olsen, A., Våge, K., Moore, G.W.K., Yashayaev, I., Jeansson, E. & Rajasakaren B.: Irminger Sea
541 deep convection injects oxygen and anthropogenic carbon to the ocean interior. *NATURE*
542 *COMMUNICATIONS* | 7:13244 |
543 DOI:10.1038/ncomms13244|www.nature.com/naturecommunications, 2016.

544 Gaillard, F., Reynaud, T., Thierry, V., Kolodziejczyk, N., & Von Schuckmann, K.: In situ-based reanalysis
545 of the global ocean temperature and salinity with ISAS: Variability of the heat content and steric
546 height. *Journal of Climate*, 29(4), 1305–1323. <https://doi.org/10.1175/JCLI-D-15-0028.1>, 2016.

547 Gill, A. E. (1982), *Atmosphere-Ocean Dynamics*, vol. 30, Academic, San Diego, CA.

548

549 Good, S. A., Martin, M. J., & Rayner, N. A.: EN4: Quality controlled ocean temperature and salinity
550 profiles and monthly objective analyses with uncertainty estimates. *Journal of Geophysical*
551 *Research: Oceans*, 118(12), 6704–6716. <https://doi.org/10.1002/2013JC009067>, 2013.

552 Josey, S. A., Hirschi, J. J.-M., Sinha, B., Duchez, A., Grist, J. P., Marsh, R.: The Recent Atlantic Cold
553 Anomaly: Causes, Consequences, and Related Phenomena. *Annual Review of Marine Science*,
554 10 (1). 475-501. <https://doi.org/10.1146/annurev-marine-121916-063102>, 2018

555 Kieke, D., & Yashayaev, I.: Studies of Labrador Sea Water formation and variability in the subpolar
556 North Atlantic in the light of international partnership and collaboration. *Progress in*
557 *Oceanography*, 132, 220–232. <https://doi.org/10.1016/j.pocean.2014.12.010>, 2015a.

558 Kieke, D., & Yashayaev, I.: Studies of Labrador Sea Water formation and variability in the subpolar
559 North Atlantic in the light of international partnership and collaboration, *Progress in*
560 *Oceanography*, 132, 220–232, <https://doi.org/10.1016/j.pocean.2014.12.010>, 2015b.

561 Kolodziejczyk, N., Prigent-Mazella A., and Gaillard F. (2017). ISAS-15 temperature and salinity gridded
562 fields. *SEANOE*. <http://doi.org/10.17882/52367>

563 Lavender, K. L., Davis, R. E., & Owens, W. B.: Mid-depth recirculation observed in the interior
564 Labrador and Irminger seas by direct velocity measurements. *NATURE* |VOL 407 | 7
565 SEPTEMBER 2000 |www.nature.com, 2000.

566 Marshall, J., & Schott, F.: Open-Ocean Convection ' Theory , and Models Observations ,. *Reviews of*
567 *Geophysics*, 37(98), 1–64. <https://doi.org/10.1029/98RG02739>, 1999.

568 Ollitrault, M., & Colin de Verdière, A.: The Ocean General Circulation near 1000-m Depth, *Journal of*
569 *Physical Oceanography*, 44(1), 384–409. <https://doi.org/10.1175/JPO-D-13-030.1>, 2014.

570 Pickart, R. S., Torres, D. J. and Clarke, R. A.: Hydrography of the Labrador Sea during active

571 convection, *J. Phys. Oceanogr.*, 32, 428–457, 2002.

572 Pickart, R. S., Straneo, F., & Moore, G. W. K.: Is Labrador Sea Water formed in the Irminger basin?
573 *Deep-Sea Research Part I: Oceanographic Research Papers*, 50(1), 23–52,
574 [https://doi.org/10.1016/S0967-0637\(02\)00134-6](https://doi.org/10.1016/S0967-0637(02)00134-6), 2003.

575 Piron, A., Thierry, V., Mercier, H., & Caniaux, G.: Argo float observations of basin-scale deep
576 convection in the Irminger sea during winter 2011–2012. *Deep-Sea Research Part I:*
577 *Oceanographic Research Papers*, 109, 76–90. <https://doi.org/10.1016/j.dsr.2015.12.012>, 2016.

578 Piron, A., Thierry, V., Mercier, H., & Caniaux, G.: Gyre-scale deep convection in the subpolar North
579 Atlantic Ocean during winter 2014–2015. *Geophysical Research Letters*, 44(3), 1439–1447.
580 <https://doi.org/10.1002/2016GL071895>, 2017.

581 Rhein, M, Steinfeldt, R, Kieke, D, Stendardo, I and Yashayaev, I.: Ventilation variability of Labrador
582 Sea Water and its impact on oxygen and anthropogenic carbon: a review, *Philosophical*
583 *Transactions of the Royal Society A: Mathematical, Physical and Engineering Sciences*,
584 375(2102). 20160321. [doi:10.1098/rsta.2016.0321](https://doi.org/10.1098/rsta.2016.0321), 2017.

585 Schmidt, S., & Send, U.: Origin and Composition of Seasonal Labrador Sea Freshwater, *Journal of*
586 *Physical Oceanography*, 37(6), 1445–1454. <https://doi.org/10.1175/JPO3065.1>, 2007.

587 Straneo, F, Pickart, R.S., Lavender, K.: Spreading of Labrador sea water: an advective-diffusive study
588 based on Lagrangian data. *Deep-Sea Research Part I-Oceanographic Research Papers*. 50:701-
589 719, 2003.

590 Swingedouw, D., Rodehacke, C. B., Behrens, E., Menary, M., Olsen, S. M., & Gao, Y.: Decadal
591 fingerprints of freshwater discharge around Greenland in a multi-model ensemble, 695–720.
592 <https://doi.org/10.1007/s00382-012-1479-9>, 2013.

593 Yang, Q., Dixon, T. H., Myers, P. G., Bonin, J., Chambers, D., & Van Den Broeke, M. R.: Recent
594 increases in Arctic freshwater flux affects Labrador Sea convection and Atlantic overturning
595 circulation, *Nature Communications*, 7, 1–7. <https://doi.org/10.1038/ncomms10525>, 2016.

596 Yashayaev, I., Bersch, M., & van Aken, H. M.: Spreading of the Labrador Sea Water to the Irminger
597 and Iceland basins, *Geophysical Research Letters*, 34(10), 1–8.
598 <https://doi.org/10.1029/2006GL028999>, 2007.

599 Yashayaev, I., & Clarke, A.: Evolution of North Atlantic Water Masses Inferred From Labrador Sea
600 Salinity Series, *Oceanography*, 21(1), 30–45. <https://doi.org/10.5670/oceanog.2008.65>, 2008.

601 Yashayaev, I., & Loder, J. W.: Recurrent replenishment of Labrador Sea Water and associated
602 decadal-scale variability, *Journal Geophysical Research: Oceans*, 121, 8095–8114,
603 <https://doi.org/10.1002/2016JC012046>, 2016.

604 Yashayaev, I., & Loder, J. W.: Further intensification of deep convection in the Labrador Sea in 2016.
605 *Geophysical Research Letters*, 44(3), 1429–1438. <https://doi.org/10.1002/2016GL071668>, 2017.

606

607

608

609

610

611

612

613

614

615

616

617

618

619

620

621

622

623

624

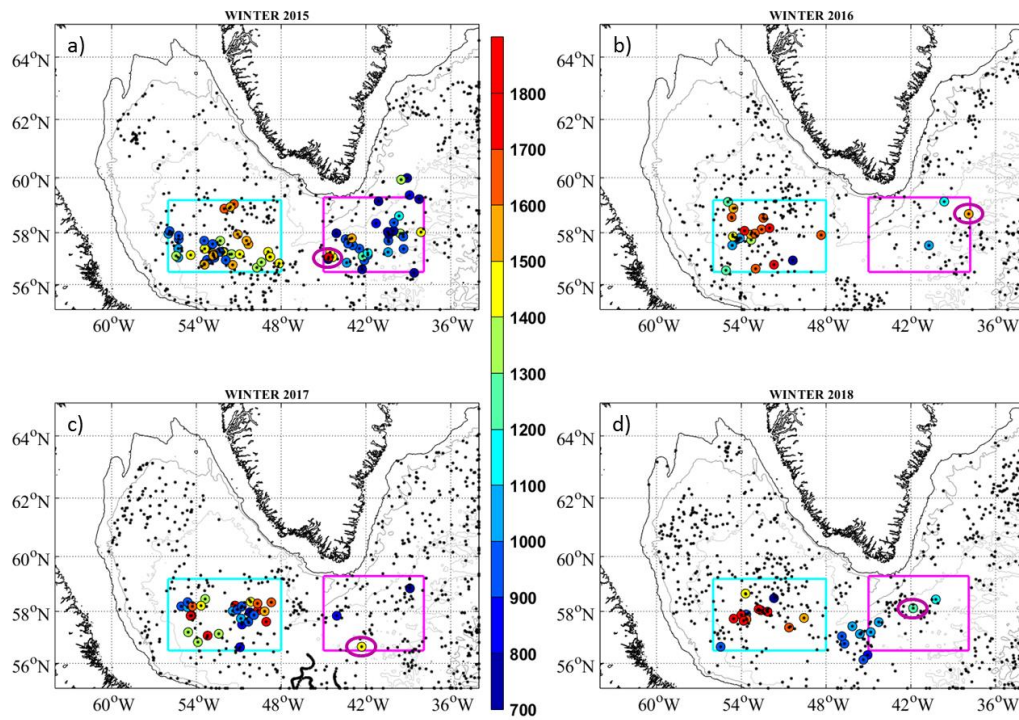
625 Table 1. Properties of the deep convection SECF and in the Labrador Sea in winters 2015 – 2018. We
 626 show: the maximal MLD observed, the aggregate maximum depth of convection, the σ_0 , S and θ of
 627 the winter mixed layer formed during the convection event and n, which is the number of Argo
 628 profiles indicating deep convection. The uncertainties given with σ_0 , S and θ are the standard
 629 deviation of the n values considered to estimate the mean values.

SECF	Maximal MLD (m)	Aggregate max. depth of convection (m)	σ_0	Salinity	θ	n
W2015	1710	1205	27.733 ± 0.007	34.866 ± 0.013	3.478 ± 0.130	29
W2016	1575	1471	27.746 ± 0.002	34.871 ± 0.003	3.388 ± 0.032	3
W2017	1400	1251	27.745 ± 0.007	34.868 ± 0.007	3.364 ± 0.109	3
W2018	1300	1300	27.748 ± 0.001	34.859 ± 0.003	3.263 ± 0.031	2
LABRADOR SEA	Maximal MLD	Aggregate max. depth of convection (m)	σ_0	Salinity	θ	n
W2015	1675	1504	27.733 ± 0.009	34.842 ± 0.010	3.279 ± 0.036	41
W2016	1801	1620	27.743 ± 0.006	34.836 ± 0.010	3.124 ± 0.047	18
W2017	1780	1674	27.752 ± 0.008	34.853 ± 0.009	3.172 ± 0.029	26
W2018	2020	1866	27.756 ± 0.006	34.855 ± 0.010	3.145 ± 0.083	13

630

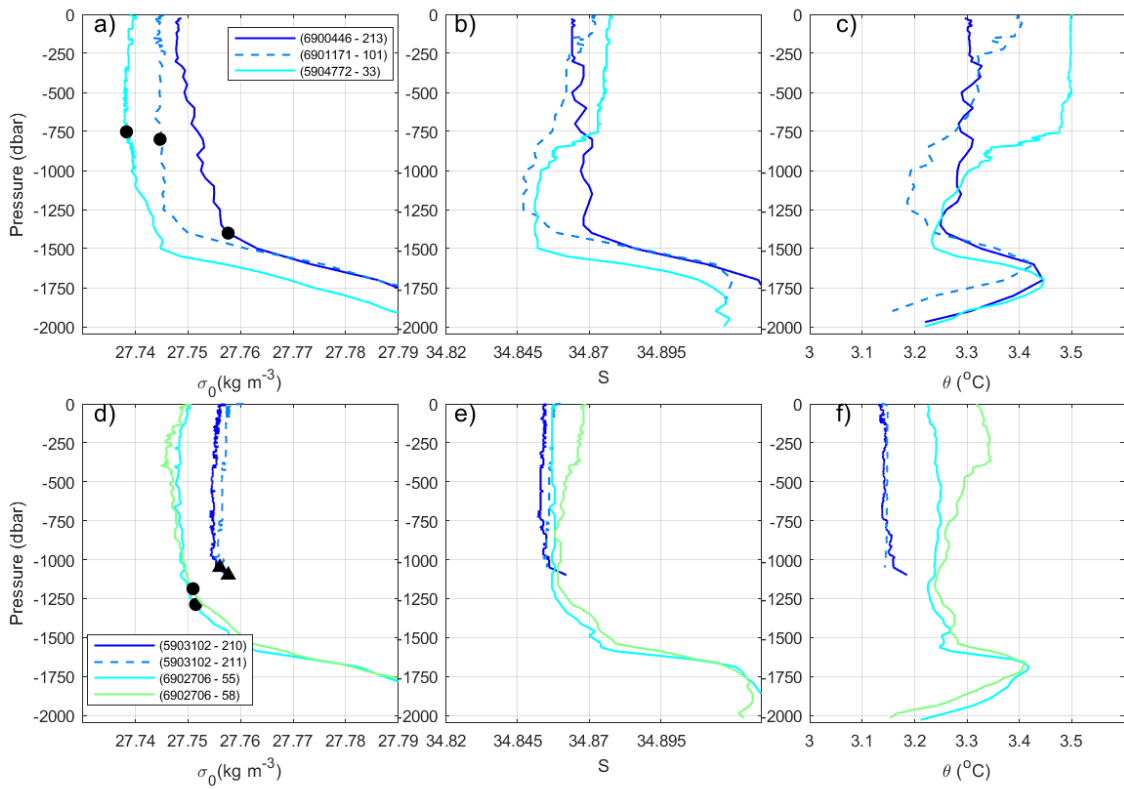
631

632



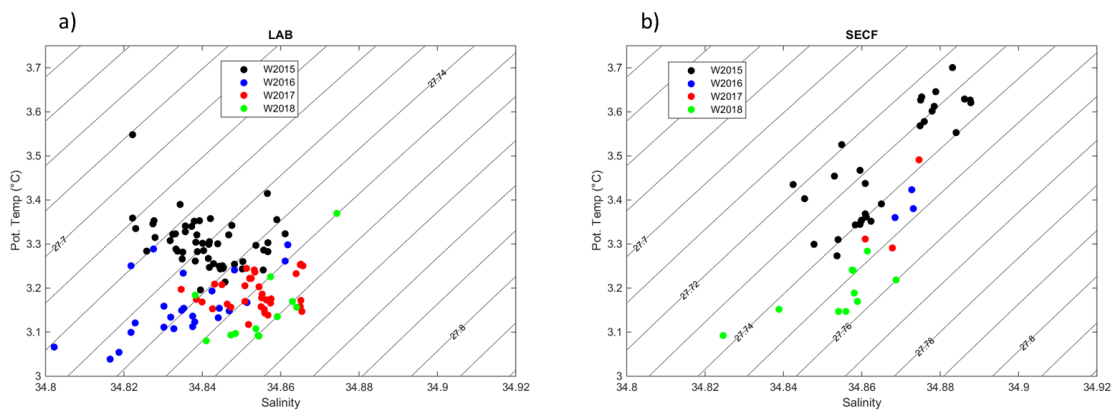
634

635 **Figure 1.** Positions of all Argo float north of 55°N in the Atlantic between 1 January and 30 April a)
 636 2015, b) 2016, c) 2017 and d) 2018 (black and colored points). The colored points and color bar
 637 indicate the mixed layer depth (MLD) when MLD was deeper than 700 m. The pink circles indicate
 638 the position of the maximal MLD observed SECF each winter. The pink and cyan boxes delimit the
 639 regions used for estimating the time series of atmospheric forcing and the vertical profiles of
 640 buoyancy to be removed in the SECF region and the Labrador Sea, respectively (SECF: 56.5°N –
 641 59.3°N and 45.0°W – 38.0°W, Labrador Sea: 56.5°N – 59.2°N and 56°W – 48°W).



642

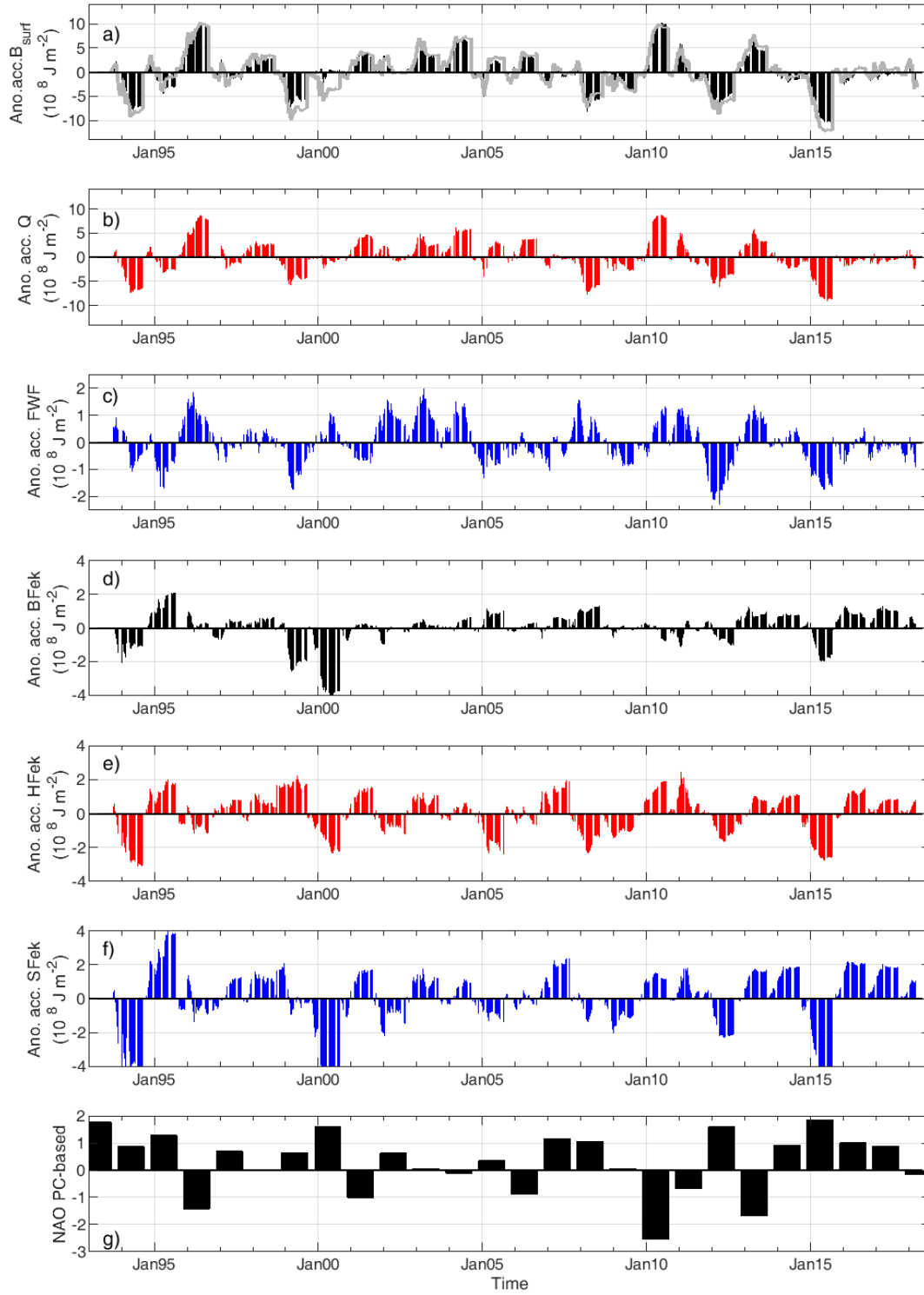
643 **Figure 2.** Vertical distribution of σ_0 , S and θ of Argo profiles showing MLD deeper than 700 m SECF in
 644 Winter 2017 (a, b and c) and in Winter 2018 (d, e, f). The black points indicate the MLD. The triangles
 645 in d) are the MLD which coincided with the maximal profiling pressure reached by the float. In the
 646 legend, the float and cycle of each profile are indicated.



647

648 **Figure 3.** TS diagrams in the mixed layer for profiles with MLD deeper than 700 m during winters
 649 2015, 2016, 2017 and 2018 for a) the Labrador Sea and b) SECF. The properties of the mixed layers
 650 were estimated as the vertical means between 200 m and the MLD.

SE CAPE FAREWELL

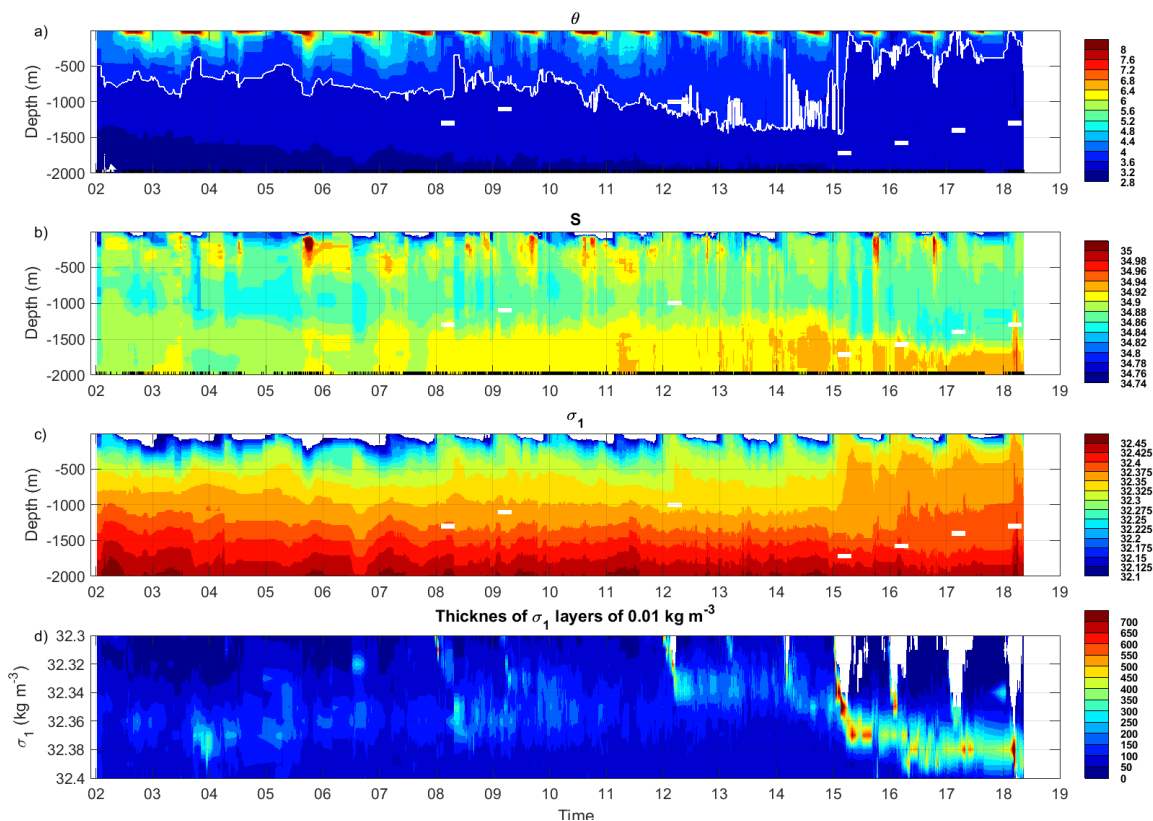


651
652

Figure 4. Time series of anomalies of accumulated a) B_{surf} , b) Q , c) FWF^* d) BF_{ek} , e) HF_{ek} and f) SF_{ek} ,

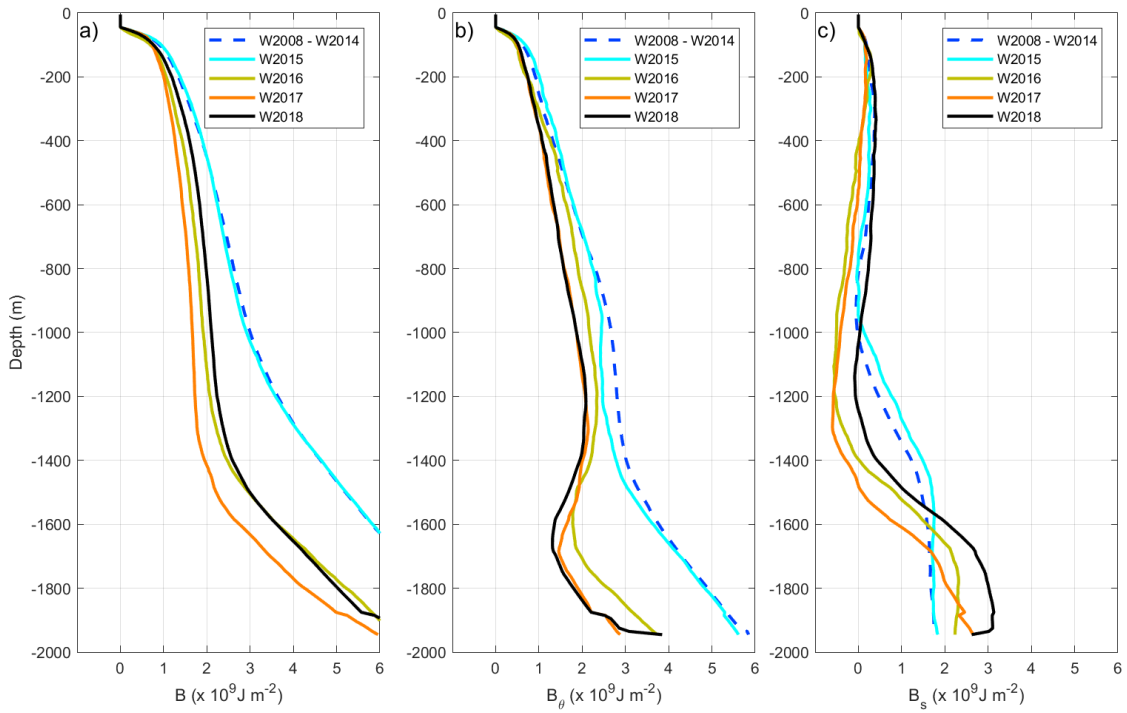
653 averaged in the SECF region. They are anomalies with respect to 1993 – 2016. The accumulation was
 654 from 1 September to 31 August the following year. The winter NAO index (Hurrell et al., 2018) is also
 655 represented in g). Gray line in a) is the sum of the anomalies of accumulated B_{surf}^* and BF_{ek} . Note that
 656 the range of values in the y-axis is not the same in all the plots.

657



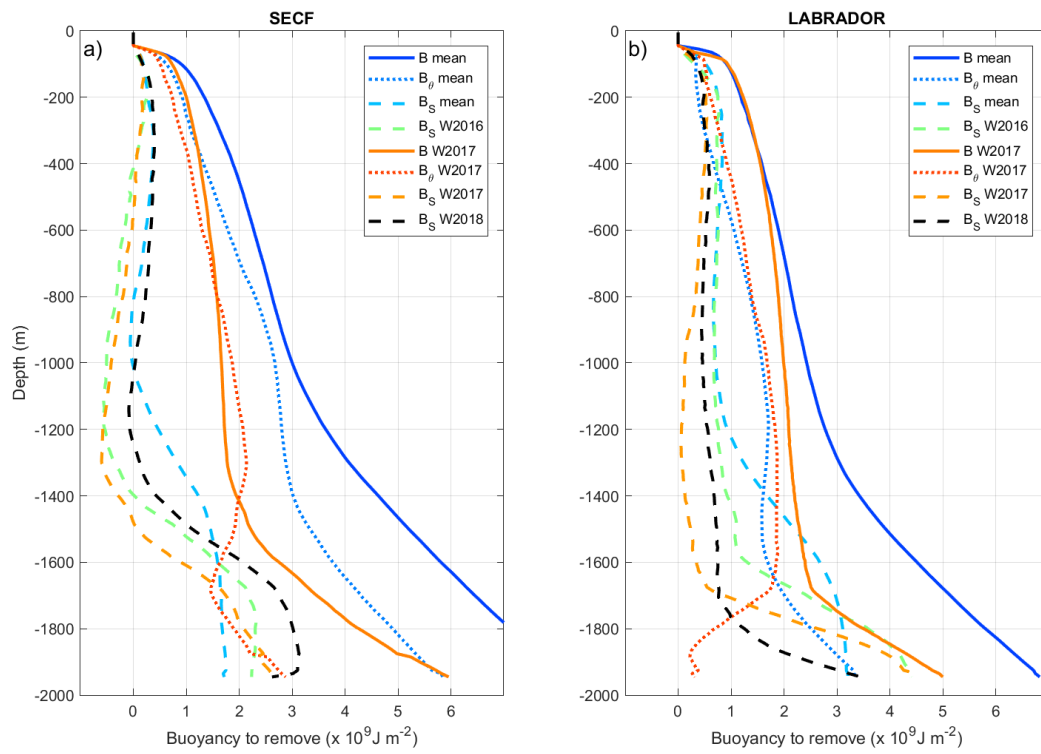
658 **Figure 5.** Time-evolutions of vertical profiles measured from Argo floats in the SECF region: a) θ ; b) S ;
 659 c) σ_1 and d) thickness of 0.01 kg m^{-3} thick σ_1 layers. The white horizontal bars in plots a), b) and c)
 660 indicate the maximal convection depth observed in Irminger Sea or SECF when deep convection
 661 occurred. The white line in plot a) indicates the depth of the isotherm $3.6 \text{ }^\circ\text{C}$. The black vertical ticks
 662 on the x-axes of plot b) indicate times of Argo measurements. These figures were created from all
 663 Argo profiles reaching deeper than 1000 m in the SECF region ($56.5^\circ - 59.3^\circ\text{N}$, $45^\circ - 38^\circ\text{W}$, pink box in
 664 Fig. 1). The yearly numbers of Argo profiles used in this figure are shown in Fig. S5.
 665

666



667

668 **Figure 6.** Vertical profile of a) the buoyancy to be removed (B), b) the thermal component (B_θ) and c)
 669 the salinity component (B_s). They were calculated from all Argo data measured in the SECF box (see
 670 Fig. 1) in September before the winter indicated in the legend. For W2015 and W2018, we
 671 considered data from 15/08/2017 to 30/09/2017 because not enough data were available in
 672 September. The number of Argo profiles taken into account to estimate the B profiles was more than
 673 ten for all the winters.



674

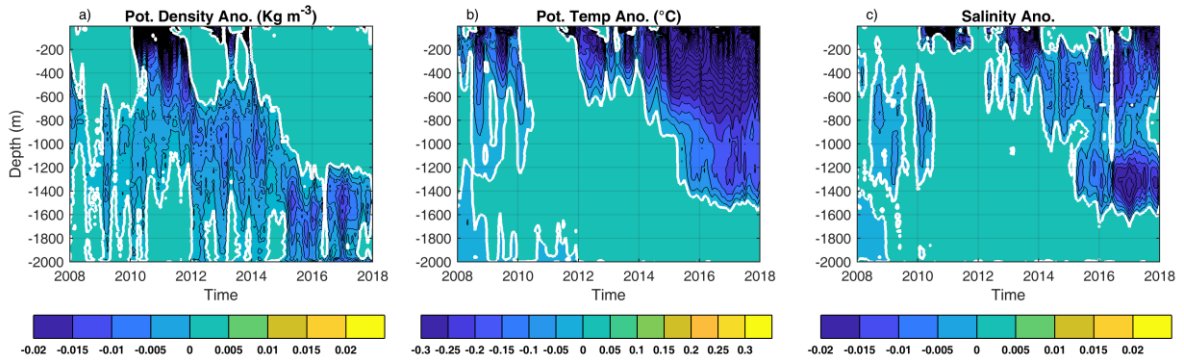
675 Figure 7. Decomposition of profiles of buoyancy to be removed (B, continuous lines) in its thermal
 676 (B_θ , dotted lines) and salinity (B_s , dashed lines) components in a) the SECF region; b) the Labrador
 677 Sea. The B_s components for W2016 and W2018 were added to show the evolution of the depth of
 678 the deep halocline.

679

680

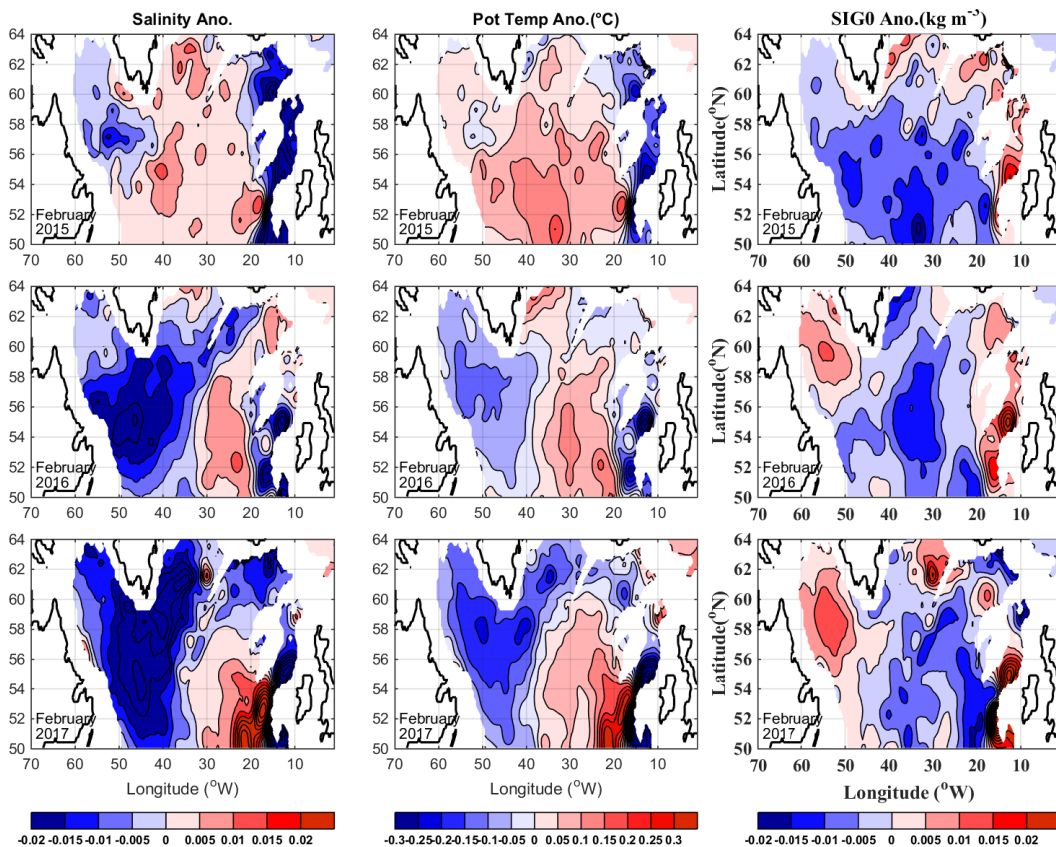
681

(58°N - 40°W)



682

683 **Figure 8.** Evolution of vertical profiles of monthly anomalies of a) σ_0 , b) θ and c) S, at 58°N, 40°W. The
684 anomalies were estimated from the ISAS database (Gaillard et al., 2016), and were referenced to the
685 monthly mean estimated for 2002 – 2016.



686

687 **Figure 9.** Horizontal distribution of the anomalies of S (left panels), θ (central panels) and σ_0 (right
688 panels) in the layer 1200 – 1400 m in February 2015 (upper panels), February 2016 (central panels)
689 and February 2017 (lower panels). The monthly anomalies were estimated from ISAS database and
690 are referenced to the period 2002 – 2016.